Reversible Hydrogen Storage via Titanium-Catalyzed $LiAlH_4$ and Li_3AlH_6

Jun Chen,* Nobuhiro Kuriyama, Qiang Xu, Hiroyuki T. Takeshita, and Tetsuo Sakai

Special Division of Green Life Technology, National Institute of Advanced Industrial Science and Technology (AIST), Ikeda, Osaka 563-8577, Japan

Received: June 5, 2001; In Final Form: August 29, 2001

A vibrating-mill technique, which can activate the reaction system by bringing the reagents into very close contact at the preparative scale and by providing extra mechanical energy, much more effectively than the well-known ball-milling method, was used to prepare titanium(III) chloride ($TiCl_3$·1/3$AlCl_3$)-doped lithium tetrahydridoaluminate ($LiAlH_4$) and lithium hexahydridoaluminate (Li_3AlH_6) powders with nanocrystallites. The phase structure and dehydriding/rehydriding properties were characterized by using X-ray diffraction (XRD), scanning electron microscopy (SEM), thermogravimetry (TG), and differential scanning calorimetry (DSC). The mechanism of reversible dehydrogenation and rehydrogenation was examined by means of X-ray photoelectron spectroscopy (XPS). Thermodynamic and kinetic measurements showed a distinct change for the dehydriding/rehydriding reactions over the temperature range 25−250 °C. From the Arrhenius plot of hydrogen desorption kinetics, apparent activation energies were found to be 42.6 and 54.8 kJ/mol H_2 for the hydride decompositions of $LiAlH_4$ and Li_3AlH_6, respectively. The results based on the properties of reversible hydrogen storage and catalysis function indicate that both the homogeneous distribution of Ti-catalyzed nanocrystalline complex hydrides and the Ti-catalyst with a $Ti^0 \leftrightarrow Ti^{3+}$ ($Ti^0/Ti^{2+}/Ti^{3+}$) defect site play important roles in optimizing the reversible hydrogen storage.

1. Introduction

The storage of hydrogen in metals/alloys[1,2] or other systems such as complexes[3−6] and advanced carbons[7] has been the subject of intensive research for many years. Apart from the utilization in nickel/metal hydride (Ni/MH) batteries,[8] no hydride system has been found to meet all the demands required for commercial vehicular applications. Nowadays, the most important work in the hydrogen storage field would be enhancing the kinetics of current hydrides and looking into new material combinations which exhibit high volumetric/gravimetric hydrogen capacity as magnesium-based hydrides and fast kinetics at low temperatures as $LaNi_5$ system.[9]

Complex hydrides with the general formula $A_xM_yH_z$, where A is an alkali or alkaline earth metal and M is a nontransition or transition metal, have been synthesized and characterized by different methods.[3−6,10] In general, the family of nontransition complex hydrides consists of A^+ cations and MH_4^- anions, where the H atoms are tetrahedrally coordinated around the M atom and have a distinct electron-rich character.[11] Because they contain lightweight elements such as lithium, sodium, and aluminum, nontransition complex hydrides (such as $LiAlH_4$[12] and Li_3AlH_6[13]) offer the potential of much higher hydrogen capacities than the intermetallic hydrides. However, hydride formation and decomposition in these complex hydrides are barely reversible, thereby making them impractical for industrial applications. Until recently, this situation has been changed by Bogdanovic et al.[14] who pioneered the demonstration that upon doping with selected titanium compounds, the dehydriding of $NaAlH_4/Na_3AlH_6/Na_2LiAlH_6$ could be kinetically enhanced and rendered reversible under moderate conditions in the solid state. This breakthrough has been followed by further progress in the development of catalysts for the reversible dehydriding of $NaAlH_4$.[15,16] It now appears that titanium halide catalysts and dry doping procedures are showing promise, especially in overcoming the high catalyst weight, low capacity, and contamination problems observed in the alkoxide catalysts such as titanium-*n*-butoxide ($Ti(OBu)_4$) and zirconium tetra-*n*-propoxide ($Zr(OPr)_4$). It is noteworthy that the hydrogen plateau pressure of the $Na_3AlH_6 \leftrightarrow NaH + Al + H_2$ equilibrium is less than 1 atm at temperatures below 100 °C, which reduces the available hydrogen content from 5.5 to 3.6 wt %. Although the recent progress on the preparation of Li_3AlH_6, Na_3AlH_6, and Na_2LiAlH_6 by the ball milling technique[17] eliminates the need for high temperatures and pressures that were previously required for their syntheses,[13,18,19] reversible dehydriding and rehydriding is not achieved in this system. Furthermore, a mechanistic explanation for the catalytic phenomenon is not available and sufficient kinetic enhancement of the rehydriding process is also required.

In the present paper, we want to further investigate the dehydrogenation and rehydrogenation of Ti-doped $LiAlH_4$ and Li_3AlH_6 nanocrystallites. The thermodynamic and kinetic parameters obtained from this system shed light onto the understanding of the catalyzed alanates.

2. Experimental Section

The starting materials lithium hydride (LiH, 95%), lithium aluminum hydride ($LiAlH_4$, 95%), and titanium chloride, anhydrous aluminum-reduced ($TiCl_3$·1/3$AlCl_3$, 99%) were provided by Aldrich Chemical and used as received without further purification. To prevent samples and starting powders from undergoing oxidation and/or hydroxide formation, they were stored and handled in a glovebox filled with pure argon (99.999%) in the presence of an oxygen scavenger and a drying

* Corresponding author. E-mail: j-chin@aist.go.jp.

10.1021/jp012127w CCC: $20.00
Published on Web 10/23/2001

agent of pure sodium.[20] To prepare Ti-doped $LiAlH_4$, a mixture containing 2 mol % $TiCl_3$·1/3$AlCl_3$, 98 mol % $LiAlH_4$, and 5 zircon balls of 4 mm in diameter was sealed in a stainless steel vial of 100 cm^3 internal volume, and then the vial was vigorously agitated at a Fuji Auto mixer with a frequency of 500 cycles per minute for up to 1 h. A similar milling process was performed for the experiment on the preparation of Ti-doped Li_3AlH_6, except that the $LiAlH_4$ was replaced by a stoichiometric composition of 2LiH + $LiAlH_4$ and a higher milling frequency of 2000 cycles per minute was used.

Structure and phase impurity on all samples in this investigation was analyzed by powder X-ray diffraction (XRD) using a Rigaku INT-2000 X-ray generator. Powders were coated with liquid paraffin oil, smeared on a glass substrate, and covered by an adhesive tape on the surface to prevent the sample from reacting with oxygen and moisture during the measuring process. The X-ray intensity was measured over a diffraction 2θ angle from 5 to 85° with a velocity of 0.02° per step (2° min^{-1}). Scanning electron microscopy (SEM) of the powders was examined by using a JEOL JSM-5600 scanning electron microscope, operating at 15 kV.

Gas−solid phase kinetic and equilibrium measurements were determined volumetrically with a carefully calibrated Sieverts-type apparatus. The experiments were carried out by rapidly heating sample that was put in an evacuated vessel (a vacuum of 10^{-6} Torr) up to the desired temperature and collecting the released hydrogen in a fixed volume. The sample holders were held in a Koyo oil bath and the temperatures could be maintained constant within 1 °C at any temperature by controlling a portion of the heating current with a chromel−alumel thermocouple. The enthalpy change and apparent activation energies for hydride decompositions were obtained by plotting the Van't Hoff equation and the Arrhenius equation, respectively.

The thermogravimetry and differential thermal analyses (TG/DTA) were characterized by employing a Rigaku TG 8120 apparatus. The sample (typically 10 mg) was preequilibrated for 10 min at 25 °C and then the temperature was linearly increased to 250 °C with a ramp of 2° per minute in a slow stream of argon. To determine the influence of temperature on hydrogen desorption and absorption, differential scanning calorimetry (DSC) was performed by using a Rigaku DSC 8230HP calorimeter at a heating rate of 1 °C per minute under 4 MPa of hydrogen. To prevent hydroxide oxidation during transportation from the glovebox to TG/DTA and DSC apparatus, the sample holder was covered by round aluminum foil and very fine sodium chloride powder, and kept in an Ar-filled bottle. The oxidation state of the titanium component was analyzed with X-ray photoelectron spectroscopy (XPS) in an ESCA-3400 Shimadzu Electron Spectrometer (Mg Kα radiation of 1253.6 eV), which was equipped with a separate chamber for loading samples. The measured surface composition is an average over 0.10 cm^2 area and 20−30 Å depth. The binding energy values correspond to the carbon C 1*s* core level at 285.0 eV.

3. Results and Discussion

3.1. $TiCl_3$·1/3$AlCl_3$-Doped $LiAlH_4$. Figure 1 shows the XRD patterns of the 2 mol % $TiCl_3$·1/3$AlCl_3$ + 98 mol % $LiAlH_4$ at different milling times. Crystalline phases were identified by comparing the experimental data with JCPDS files from International Center for Diffraction Data (ICDD) ($LiAlH_4$, 12-473; $TiCl_3$, 29-1358). In Figure 1a, peaks that are attributed to the phase of monoclinic $LiAlH_4$ have been marked by *hkl* reflections, while no characteristic peaks of crystalline $TiCl_3$ (typically with 2θ =16.31°, 32.41°, and 42.34°) have been

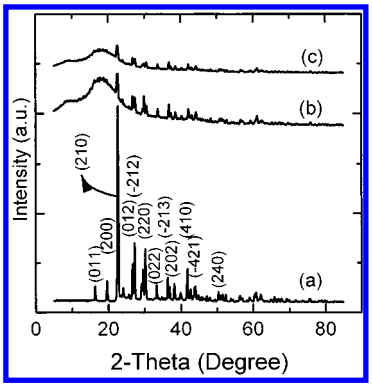

Figure 1. XRD patterns of the 2 mol % $TiCl_3$·1/3$AlCl_3$ + 98 mol % $LiAlH_4$ mixture as a function of milling time: (a) 0 h; (b) 0.5 h; and (c) 1 h.

observed, possibly owing to its relatively small content. In Figures 1b and 1c, the XRD patterns of the as-milled samples are in good agreement with that in Figure 1a, although some peaks disappeared and the *hkl* reflections were relatively broader. This result suggests that the milling procedure offer gram quantities of $LiAlH_4$ nanocrystallites. It was previously reported that polycrystalline $LiAlH_4$ was completely transformed into polycrystalline Li_3AlH_6 during short mechanochemical treatment with 3 mol % $TiCl_4$ at room temperature.[21] This difference may be a result of the various experimental conditions such as the catalyst and milling parameters.

The average coherence length of the $TiCl_3$·1/3$AlCl_3$-doped $LiAlH_4$ phase, 18 nm, calculated from the breadth of diffraction peaks by the Scherrer equation,[22] ($t = 0.89\lambda/(B \cos \theta)$, where λ is 1.54056 Å, B is the full width at half-height, and θ is the position of the selected Bragg angle), is much smaller than that of the un-doped $LiAlH_4$ phase, 200 nm. The causes of the formation of a fine grain size below 20 nm as in the vibrating-milled sample can be attributed to the following facts: (1) the high-speed vibration increases the atomic-level strain[23] and decreases the crystal size to a nanometer scale; and (2) the atomic Ti and Al were initially precipitated in segregated component phases,[24] and subsequently adhered to the surface of the remaining $LiAlH_4$ phase, and this would promote the dispersion of nano-phase during the milling process.

The generally accepted model of the thermal decomposition of $LiAlH_4$ involves three reactions as described in eqs 1, 2, and 3.[25,26] These equations are characterized by very slow kinetics and reversibility only under severe conditions:

$$3LiAlH_4 \rightarrow Li_3AlH_6 + 2Al + 3H_2 \quad (1)$$

$$Li_3AlH_6 \rightarrow 3LiH + Al + {}^3/_2H_2 \quad (2)$$

$$3LiH \rightarrow 3Li + {}^3/_2H_2 \quad (3)$$

The first two of these reactions proceed around 160−210 °C and liberate 5.3 and 2.6 wt % of hydrogen, respectively. The dehydrogenation of LiH occurs only at very high temperatures and is therefore normally not considered as a source of hydrogen available from $LiAlH_4$.

Figure 2 shows the TG/DTA results of the 2 mol % $TiCl_3$·1/3$AlCl_3$ + 98 mol % $LiAlH_4$ mixture before and after l hour of milling. It can be seen that within the examined temperature range, hydrogen desorbs from these two samples with rather different behavior. In the case of the un-milled sample, the desorption of hydrogen started at 160 °C and ended at 220 °C, showing two obvious regions for hydride decomposition: one

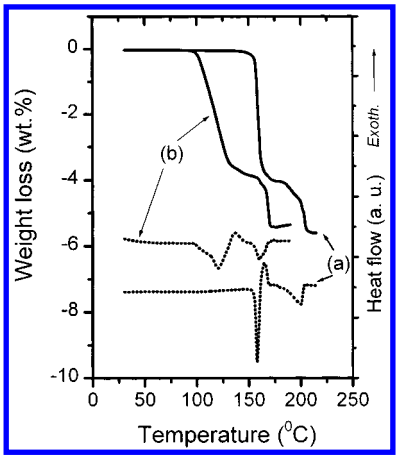

Figure 2. TG (full curves) and DTA (dotted curves) of the 2 mol % $TiCl_3$·1/3$AlCl_3$ + 98mol % $LiAlH_4$ mixture: (a) un-milled, and (b) as-milled for 1 h.

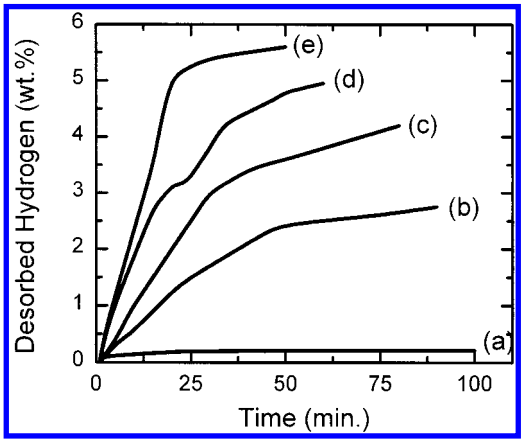

Figure 3. The amount of desorbed H_2 versus time. (a) Initial $LiAlH_4$ at 100 °C, and the 2 mol % $TiCl_3$·1/3$AlCl_3$-doped $LiAlH_4$ nanocrystallites at (b) 100 °C, (c) 125 °C, (d) 150 °C, and (e) 175 °C.

is around the temperature of about 165 °C and the other at about 195 °C. These two steps correspond to eqs 1 and 2, respectively. In the case of the milled sample, the starting temperature of hydrogen desorption is around 100 °C, and the whole hydride decomposition shifts by about 60 °C toward lower temperatures, indicating an enhanced kinetic effect made possible by the catalyst.

Figure 3 shows the hydrogen desorption rate measurements at different temperatures for the $TiCl_3$·1/3$AlCl_3$-doped $LiAlH_4$. The desorption rates are related to the heating temperatures. In addition, the desorption curves change from an initial sigmoidal shape to a decreasing feature, except the discontinuity in desorption curve at 150 °C due to the combination of two stages for hydride decompositions. This behavior indicates that the rate-controlling step contains nucleation and diffusion as well as heat transfer. Moreover, the kinetics of dehydriding can be described by first-order reaction rate after fitting the experimental data. The temperature dependence of k can be correlated by the Arrhenius equation,[27] $k = A \exp(-E/RT)$, where A is a temperature-independent coefficient, E is the apparent activation energy for hydride decomposition, R is the gas constant, and T is absolute temperature. The natural logarithm of this equation yields a first-order linear equation on $1/T$, and the plot of ln k vs $1/T$ is shown in Figure 4. The apparent activation energy was measured to be 42.6 kJ/mol H_2 and the coefficient is 2.5 $\times$ 10^{10} wt % per min. These values are lower than that reported for the Ti-doped $NaAlH_4$,[28] suggesting that the particle size reductions can improve the desorption kinetics. As a result, the

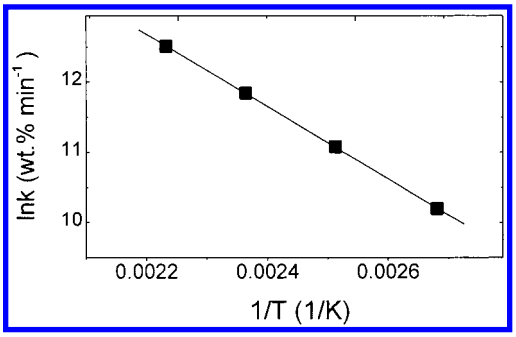

Figure 4. The ln k versus reciprocal temperature of the 2 mol % $TiCl_3$·1/3$AlCl_3$-doped $LiAlH_4$ powders, where k is the hydrogen desorption amount with the unit of wt % min^{-1}.

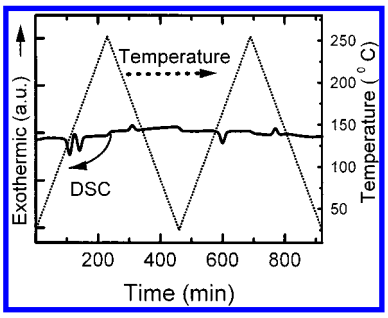

Figure 5. DSC analysis of the 2 mol % $TiCl_3$·1/3$AlCl_3$-doped $LiAlH_4$ nanocrystallites at the first two heating/cooling cycles.

rate equation of the hydride decomposition of $TiCl_3$·1/3$AlCl_3$-doped $LiAlH_4$ can be expressed in the following equation:

$$k = 2.5 \times 10^{10} \exp(-5120/T) \qquad (4)$$

As discussed above, the $TiCl_3$·1/3$AlCl_3$-doped $LiAlH_4$ can be thermally decomposed at reasonable temperatures. More significantly, the reversible dehydriding/rehydriding reactions of this system have been achieved as evidenced in Figure 5. In the first heating step, two endothermic peaks were observed at 135 °C and 165 °C, owing to the hydride decompositions as described in eqs 1 and 2, respectively. Upon cooling, an exothermic peak was detected around 175 °C, signaling that a rehydrogenation occurred. When this sample was exposed to a subsequent heating and cooling cycle, an endotherm upon heating as well as an exotherm upon cooling was detected, revealing that the dehydriding/rehydriding reaction proceeded reversibly. After these two DSC cycles, the TG analysis was performed and a maximum value of 1.8 wt % hydrogen was observed. From previous thermal analysis,[26] it has been known that Li_3AlH_6 is more stable than $LiAlH_4$. Thus, Li_3AlH_6 should have a lower equilibrium pressure of hydrogen, which suggests an easier rehydrogenation process. Therefore, the exothermic peak, as noted in Figure 5, belongs to the reabsorption of hydrogen from LiH and Al into an intermediate phase such as Li_3AlH_6. In other words, eq 2 is reversible under a hydrogen pressure of 4 MPa. To our knowledge, this is the first time that $TiCl_3$·1/3$AlCl_3$-doped $LiAlH_4$ has been shown to successfully decompose and *re-absorb* hydrogen under the conditions of classical metal hydrides. Although its hydrogen capacity is somewhat lower than expected, possibly due to the low pressure (4 MPa of hydrogen) as well as the short reaction time that reduces the hydrogen availability, the dehydriding/rehydriding reversibility with 1.8 wt % of hydrogen is still very attractive.

3.2. $TiCl_3$·1/3$AlCl_3$-Doped Li_3AlH_6. The doping procedure of preparing catalyzed complex hydrides has been proven to play an important role in developing and optimizing the

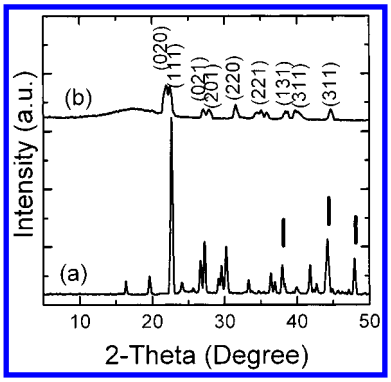

Figure 6. XRD patterns of 2 mol % $TiCl_3 \cdot 1/3AlCl_3$ + 98 mol % stoichiometric composition of 2LiH + $LiAlH_4$: (a) before milling and (b) after milling for 1 h. In the initial mixture, the peaks related to LiH are marked by bars and the others are related to $LiAlH_4$ (JCPDS file No. 12-473). In the sample as-milled, peaks attributed to the monoclinic Li_3AlH_6 phase are marked according to JCPDS file No. 27-282.

reversible hydrogen storage system. On the other hand, Li_3AlH_6 has a relatively higher hydrogen capacity than that of Na_3AlH_6, and a lower plateau pressure than that of $LiAlH_4$ and thereby was selected to prepare Ti-doped complex hydrides by the high-energy milling technique. The influence of phase change on the dehydriding/rehydriding properties was also studied for the aim of clarifying the relation between the reversible hydrogen storage and catalysis function.

The color of the 2 mol % $TiCl_3 \cdot 1/3AlCl_3$ + 98 mol % stoichiometric composition of 2LiH + $LiAlH_4$ sample after 1 h of milling was deep gray rather than light gray for the initial mixture, and this color change may suggest a solid-state reaction possibly occurred. Figure 6 shows the XRD patterns of these two powders, viz., before and after milling. Interval experimental analyses demonstrate that after 1 h of milling the initial LiH and $LiAlH_4$ phases have been mostly used up to synthesize Li_3AlH_6 with a monoclinic crystal structure. This result, along with the reported data,[17] confirmed that the solid-state reaction in eq 5 could proceed through mechanical alloying:

$$2\ \text{mol \%}\ TiCl_3 \cdot 1/3AlCl_3 + 98\ \text{mol \%}\ (2LiH + LiAlH_4) \rightarrow \text{Ti-doped}\ Li_3AlH_6 \quad (5)$$

Simultaneously, it is very clear that the diffraction peaks of the milled phase are significantly broadened, resulting mainly from the fine grain size. The average coherence length was 20 nm, which is much smaller than that of the initial LiH or $LiAlH_4$ phase. This is further confirmed by the observations of SEM (Figure 7). The cause of the formation of a fine grain size around 20 nm in the milled sample can be attributed to these facts: (1) for the decomposition reaction of $LiAlH_4$ into Li_3AlH_6, Al, and H_2, the standard Gibbs free energy (ΔG°_{298K}) is −27.7 kJ/mol;[29] (2) the high-speed milling technique can activate the reaction system by providing extra mechanical energy;[30] and (3) $TiCl_3$ was partially consumed by reaction with $LiAlH_4$ to give undetermined, reduced Ti phase and nanocrystalline Al and Ti_x-Al_y phases, which enhances the dispersion for nano-phase, as discussed in Section 3.1.

The effect of the Ti doping of nanocrystalline Li_3AlH_6 on the thermodynamic parameter for hydrogen desorption was also monitored. Figure 8 shows the hydrogen pressure as a function of time for hydride decomposition at various temperatures (100 °C, 125 °C, 150 °C, and 175 °C). When heated at 125 °C, a large portion of hydrogen was released from the $TiCl_3 \cdot 1/3AlCl_3$-doped Li_3AlH_6 due to the hydride decomposition as described

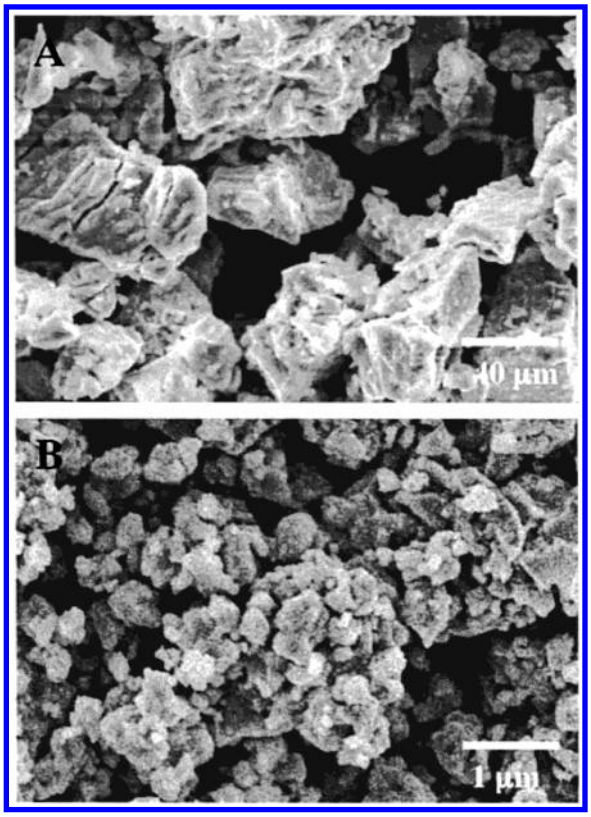

Figure 7. SEM images showing the morphologic change of (a) the bulk phases (the initial 2LiH + $LiAlH_4$ mixture) to (b) Li_3AlH_6 nanocrystallites.

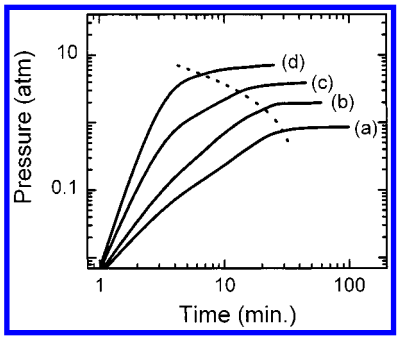

Figure 8. Equilibrium hydrogen desorption pressures of $TiCl_3 \cdot 1/3AlCl_3$-doped Li_3AlH_6 at (a) 100 °C, (b) 125 °C, (c) 150 °C, (d) 175 °C.

in eq 2. Heating to higher temperature causes a further desorption of hydrogen. Linear extrapolation of the low-pressure and the high-pressure sections in each curve gave rise to an intersection of these two lines. The pressure values at the intersection points corresponding to different temperatures can be considered as the dissociation pressures of Li_3AlH_6, which were given as (T (°C), P (atm)): 100, 0.86; 125, 1.91; 150, 3.8; 175, 7.0. Based on the dissociation plateau pressures at given temperatures, a plot of ln P versus $1/T$ (Figure 9) is a straight line ($\ln P = -4915.1/T + 13.01$) with its slope being a measure of enthalpy change (ΔH) that is 41.1 kJ/mol H_2. This is a very interesting finding because it is much lower than the enthalpy change measured by thermal analysis (~100 kJ/mol H_2).[31] This result indicates that $TiCl_3 \cdot 1/3AlCl_3$-doped nanocrystalline Li_3AlH_6 decomposes easily at lower temperatures than the ordinary polycrystalline material.

Figure 10 shows the temperature effects on hydrogen desorption kinetics of the $TiCl_3 \cdot 1/3AlCl_3$-doped Li_3AlH_6. It is evident that the shape of the desorption curve changes signifi-

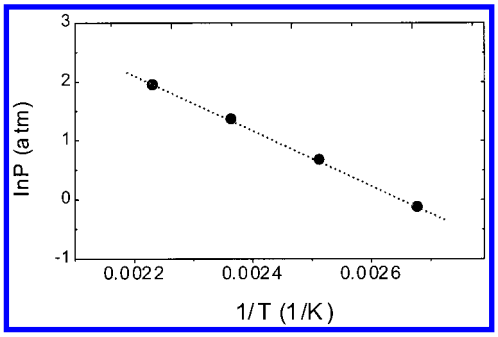

Figure 9. Van't Hoff diagram showing equilibrium hydrogen pressures over temperatures for $TiCl_3$·1/3$AlCl_3$-doped Li_3AlH_6.

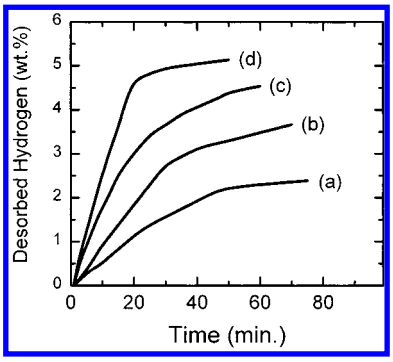

Figure 10. The amounts of hydrogen desorption versus time for $TiCl_3$·1/3$AlCl_3$-doped Li_3AlH_6 at (a) 100 °C, (b) 125 °C, (c) 150 °C, and (d) 175 °C.

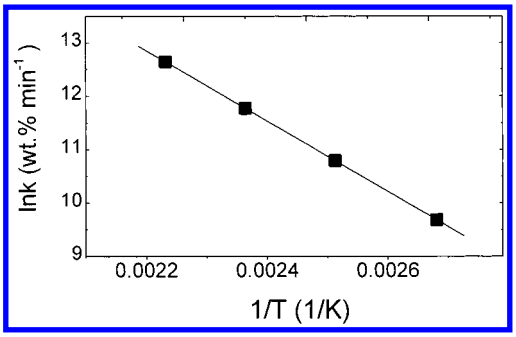

Figure 11. The ln k versus reciprocal temperature of the $TiCl_3$·1/3$AlCl_3$-doped Li_3AlH_6, where k is the hydrogen desorption amount with the unit of wt % min^{-1}.

cantly with increasing temperature. This is most likely associated with changes in the rate-limiting step of desorption. Figure 11 is the Arrhenius plot for the $TiCl_3$·1/3$AlCl_3$-doped Li_3AlH_6. Similarly, the apparent activation energy and the coefficient were found to be 54.8 kJ/mol H_2 and 7.3 × 10^{10} wt % per min, respectively. Thus, the dependence of hydrogen desorption rate on temperature can be described with the following equation:

$$k = 7.3 \times 10^{10} \exp(-6586/T) \qquad (6)$$

Figure 12 shows the first heating/cooling DSC analysis obtained for the $TiCl_3$·1/3$AlCl_3$, LiH, and $LiAlH_4$ mixture before and after milling. In Figure 12a, the DSC heating curve shows two endothermic peaks, one at about 175 °C and the other slightly broader peak at about 205 °C. The first peak corresponds to the hydride decomposition as shown in eq 1, whereas the second one shows its further decomposition as illustrated in eq 2. Note that no enthalpy change was observed for this sample when cooled from 250 °C to room temperature, suggesting that no rehydriding reaction is taking place. Thus, the hydrogenation is not reversible. In Figure 12b, only one endothermic peak is

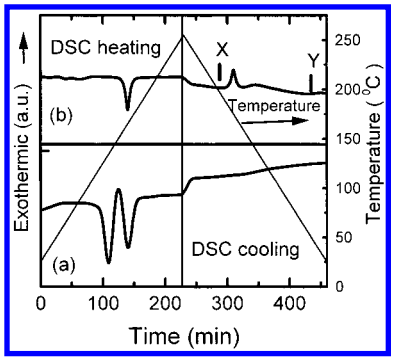

Figure 12. DSC analysis of (a) the 2 mol % $TiCl_3$·1/3$AlCl_3$ + 98 mol % (2LiH + $LiAlH_4$) mixture, and (b) the as-prepared Ti-doped Li_3AlH_6 nanocrystallites. Bars marked by X and Y indicate the places of XRD patterns that are shown in Figure 13.

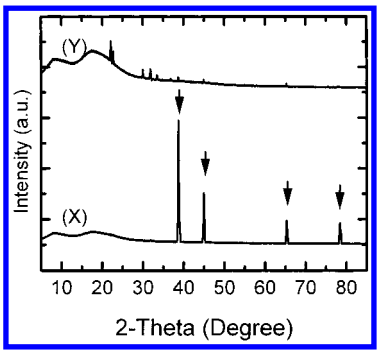

Figure 13. XRD patterns showing the rehydriding transformation of (X) LiH + Al (with H_2) to (Y) an intermediate complex hydride phase.

observed at 180 °C, and this step should result from the hydride decomposition as shown in eq 2, with a shifting about 25 °C lower than that for un-doped sample. This suggests that there is no untreated $LiAlH_4$ phase remaining in the as-milled sample. However, it is worth noting that upon cooling of the Ti-doped Li_3AlH_6, an exothermic peak was observed at 190 °C. Comparing the XRD patterns of this sample before and after the exothermic peak, as marked by X and Y in Figure 12, reveals their rather different features (Figure 13). The characteristic peaks in X pattern (Figure 13a) can be attributed to the similar structures of LiH and Al. In the Y sample after DSC cooling, the peaks owing to the LiH and Al are almost absent and small new peaks are visible. Although a structure determination was not attempted because of few peaks, we deduced that an intermediate phase such as $LiAlH_2$,[25a] Li_3AlH_6,[26] or LiAl−H[32] was formed. In other words, the reaction of eq 2 can occur reversibly or at least partially reversibly. Therefore, nanocrystalline Ti-doped Li_3AlH_6 is of fundamental interest because its attributes are substantially different from those displayed by bulk materials. This sample was subjected to five subsequent heating and cooling cycles. The endotherm around 180 °C as well as the exotherm around 190 °C persisted, but the exotherm became relatively broader, exhibiting that the reversible hydriding/dehydriding reaction proceeds but with a decreasing reversibility. Importantly, the temperature of the exothermic reaction is higher than that of endotherm, which is opposite to what has been observed in the conventional intermetallic hydrides. This will be discussed in further details in the next section.

3.3. Catalytic Mechanism. In our experiment, we also selected Ti and TiH_2 to replace $TiCl_3$·1/3$TiCl_3$ as dopants. Such Ti- or TiH_2-doped $LiAlH_4$ and Li_3AlH_6 were then examined by DSC measurements under the same conditions as before. The DSC heating curves are similar to that in Figures 5 and 12. Unfortunately, the DSC cooling curves show no exothermic

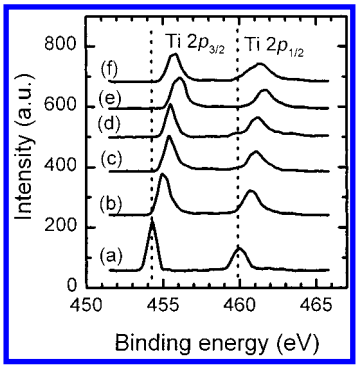

Figure 14. XPS spectra of Ti $2p_{3/2}$ and Ti $2p_{1/2}$ for: (a, b, c, and d) $TiCl_3$·1/3$AlCl_3$/$LiAlH_4$ samples with the doping amount of 0.5, 1.0, 2.0, and 3.0 mol % $TiCl_3$·1/3$AlCl_3$, respectively; and a 2.0 mol % $TiCl_3$·1/3$AlCl_3$ doped sample during (e) dehydriding process of the second decomposition step and (f) rehydriding reaction.

peak, meaning that Ti and TiH_2 have not created reversible hydrogen desorption and reabsorption. To understand the nature of the Ti-catalyst, $TiCl_3$·1/3$AlCl_3$-doped $LiAlH_4$ was studied in depth by XPS analysis. Figure 14 shows the effect of $TiCl_3$·1/3$AlCl_3$ loading on XPS profiles. It is apparent that the shape of the XPS spectra and the binding energy values of Ti $2p_{3/2}$ and Ti $2p_{1/2}$ have been greatly changed by adding amounts of $TiCl_3$·1/3$AlCl_3$ up to 2 mol %. Since similar results (XPS shape and position) have been obtained in the samples with 2−3 mol % $TiCl_3$·1/3$AlCl_3$ loading amounts, we define that the content of 2 mol % $TiCl_3$·1/3$AlCl_3$ addition is the saturated loading capacity, which can produce a homogeneous catalyzed layer on the inside $LiAlH_4$ surface. An increase of the amount of titanium precursor larger than this saturated loading capacity will decrease the hydrogen storage efficiency.

Four aspects warrant discussion in order to explain its catalytic function. First, despite efforts to investigate the photocatalysis of the Ti^{3+}/Ti^{4+} defect site,[33,34] little information is available on the catalytic mechanism in complex hydrides. The shape of the XPS spectra in Figure 14 shows that the $Ti^0 \Leftrightarrow Ti^{3+}$ ($Ti^0/Ti^{2+}/Ti^{3+}$) defect site with electron attacking is observed during the dehydriding and rehydriding reactions. The core level of Ti $2p_{3/2}$ for standard Ti^0 and Ti^{3+} is located at 454.0 and 457.4 eV.[33,35] However, in the sample after the first dehydriding step (Figure 14e), the Ti $2p_{3/2}$ core level is located at 456.0 eV. After rehydrogenation (Figure 14f), the Ti $2p$ spectrum is slightly broadened and a shoulder band appears 0.5 eV lower than the binding energy of the sample in the dehydriding stage. In addition, the band curve is asymmetric with a tail at the lower binding energy side. These data fall between the two standard values, suggesting that the surface of $TiCl_3$·1/3$AlCl_3$-doped sample contain Ti^{3+}, Ti^{2+}, as well as Ti^0. Typically, this behavior is much clearer in the rehydrogenation process.

Second, the model for hydrogen storage of Ti-doped complex hydrides is based on Ti-catalyzed thermal decomposition and recombination of several phases but not on incorporation of hydrogen atoms occupying the octahedral or/and tetrahedral sites in metal hydrides.[36] In the latter case, the hydrogen desorption and absorption normally cause lattice expansion without altering the mother-alloy structure. However, in the dehydriding process of the alkali nontransition metal complex hydrides, new phases such as $LiAlH_4$ to Li_3AlH_6, Li, and Al appeared. In the rehydriding process, the reaction involves in the conglomeration of several solid phases with hydrogen gas to form a homogeneous complex hydride phase. This is the reason the rehydrogenation reaction of complex hydrides still needs special conditions (high hydrogen pressure and high temperature) even

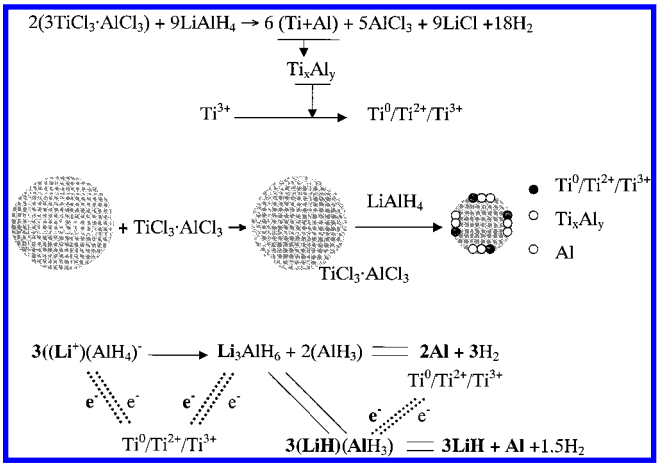

Figure 15. A tentative model of the dehydriding/rehydriding reactions catalyzed by the $Ti^0/Ti^{2+}/Ti^{3+}$ defect site.

in the presence of catalysts. As a result, at constant hydrogen pressure as measured in DSC of Figures 5 and 12, the temperature for complex hydride formation would be higher than for its decomposition.

Third, the formation of a microstructure composite with a $Ti^0/Ti^{2+}/Ti^{3+}$ defect sites results in the improvement of dehydriding kinetics. In the effort to understand the $Ti^0 \Leftrightarrow Ti^{3+}$ defect sites and its role in the catalysis function, a model was proposed as shown in Figure 15. During the doping process, the reduction of Ti^{3+} by $LiAlH_4$ proceeds with formation of reduced Ti^0 and Al phases. The milling technique provides energy for the precipitates of Ti and Al in the remaining $LiAlH_4$ phase, yielding the desired nanocrystalline powders. Defect site containing Ti^0, Ti^{2+}, and Ti^{3+} with electron attacking capability induces the activation for the dehydriding reaction. After isolating unstable AlH_3,[16,37] the phase transformation of $LiAlH_4$ to Li_3AlH_6 occurs by diffusions of aluminum and hydrogen.[38] As a result, the catalyst with the defect site leads to the formation of molecular LiH because of its high stability.[39]

Finally, the schematic diagram of Figure 15 also shows a possible pathway leading to the formation of multiple core nanocomposites, which enhances kinetics for the reversible rehydriding reaction. These composite nanoparticles would then react with each other and with hydrogen facilitated by the $Ti^0/Ti^{2+}/Ti^{3+}$ defect site, which presumably influences the affinity to chemisobed hydrogen of Al sites.[37] As suggested in two DSC measurements, both the homogeneous distribution of nanocrystalline Ti-catalyst and the defect site with electron attacking capability are the prerequisites for undergoing the rehydriding reaction and forming intermediate complex hydrides. Therefore, this multiaction of the Ti-catalyst should be the key factor for the success of the reversible dehydrogenation/rehydrogenation. Further work is underway to utilize these Ti-composite nanoparticles for catalytic applications.

4. Conclusion

We have shown that the vibrating-mill technique is a successful way for producing $TiCl_3$·1/3$AlCl_3$-doped $LiAlH_4$ and Li_3AlH_6 powders with nanocrystallites. The appropriate loading amount for $TiCl_3$·1/3$AlCl_3$ as a catalyst precursor is about 2 mol %. This doping process produces a Ti-component state with a $Ti^0 \Leftrightarrow Ti^{3+}$ ($Ti^0/Ti^{2+}/Ti^{3+}$) defect site by the reduction of $TiCl_3$ with $LiAlH_4$. Such Ti-doped $LiAlH_4$ and Li_3AlH_6 exhibit good characteristics in terms of reactivity in dehydriding/rehydriding reactions. The desorption of hydrogen from the Ti-doped $LiAlH_4$ Li_3AlH_6 obeys the Arrhenius equation, from which apparent

activation energies were measured to be 42.6 and 54.8 kJ/mol H_2 for the hydride decompositions of $LiAlH_4$ and Li_3AlH_6, respectively. The rehydrogenation process is controlled by phase conglomerations induced by the nanocrystalline Ti-catalyst as well as the $Ti^0/Ti^{2+}/Ti^{3+}$ defect site. The occurrence of dehydriding/rehydriding reactions in these Ti-containing complex hydrides, which involve several catalytic phase transitions different from conventional metal hydride systems, suggests their attractive application as reversible hydrogen storage carriers.

Acknowledgment. This work was financially supported by the New Energy and Industrial Technology Development Organization (NEDO) and carried out under the World Energy Network (WE-NET) Project − International Clean Energy Technology Utilizing Hydrogen.

References and Notes

(1) (a) Alefeld, G.; Völkl, J. *Hydrogen in Metals I & II*; Springer-Verlag: Berlin, 1978. (b) Wipf, H. *Hydrogen in Metals III*; Springer-Verlag: Berlin, 1997.

(2) Schlapbach, L. *Hydrogen in Intermetallic Compounds I & II*; Springer-Verlag: Berlin, 1988 & 1992.

(3) (a) Wiswall, R. In *Hydrogen in Metals II*; Alefeld, G., Völkl, J., Eds.; Springer-Verlag: Berlin, 1978; Vol. 29, p 201. (b) Yvon, K. In *Encyclopedia of Inorganic Chemistry*; King, R. B., Ed.; John Wiley: Weinheim, 1994; Vol. 3, p 1401.

(4) Bronger, W. *Angew. Chem., Int. Ed. Engl.* **1991**, *30*, 759.

(5) Firman, T. K.; Landis, C. R. *J. Am. Chem. Soc.* **1998**, *120*, 12650.

(6) Olofsson-Mårtensson, M.; Kritikos, M.; Noréus, D. *J. Am. Chem. Soc.* **1999**, *121*, 10908.

(7) (a) Dillon, A. C.; Jones, K. M.; Bekkedahl, T. A.; Kiang, C. H.; Bethune, D. S.; Heben, M. J. *Nature* **1997**, *386*, 377. (b) Chambers, A.; Park, C.; Baker, R. T. K.; Rodriguez, N. M. *J. Phys. Chem. B* **1998**, *102*, 4253.

(8) Sakai, T.; Matsuoka, M.; Iwakura, C. In *Handbook on the Physics and Chemistry of Rare Earths*; Gschneidner, K. A., Jr., Eyring, L., Eds.; Elsevier Science: Amsterdam, 1995; Vol. 21, p 133.

(9) Sandrock, G.; Thomas, G. In *Hydride Information Center*; http://hydpark.ca.sandia.gov/; Sandia National Laboratories: Livermore, CA, 2001.

(10) Sullivan, E. A.; Wade, R. C. *Kirk-Othmer Encycl. Chem. Technol.* **1980**, *12*, 772.

(11) (a) Bulychev, B. M.; Verbetskii, V. N.; Semenenko, K. N. *Russ. J. Inorg. Chem.* **1977**, *22*, 1611. (b) Lauher, J. W.; Dougherty, D.; Herley, P. J. *Acta Crystallogr.* **1979**, *B35*, 1454. (c) Belskii, V. K.; Bulychev, B. M.; Golubeva, A. V. *Russ. J. Inorg. Chem.* **1983**, *28*, 1528.

(12) (a) Finholt, A. E.; Bond, A. C., Jr.; Schlesinger, H. I. *J. Am. Chem. Soc.* **1947**, *69*, 1199. (b) Sklar, N.; Post, B. *Inorg. Chem.* **1967**, *6*, 669.

(13) Ehrlich, R.; Young, A. R., II; Dvorak, G. R. J.; Shapiro, P.; Smith, H. F. *J. Am. Chem. Soc.* **1966**, *88*, 858.

(14) (a) Bogdanovic, B.; Schwickardi, M. *J. Alloys Compd.* **1997**, *253*−*254*, 1. (b) Bogdanovic, B.; Brand, R. A.; Marjanovic, A.; Schwickardi, M.; Tolle, J. *J. Alloys Compd.* **2000**, *302*, 36.

(15) (a) Jensen, C. M.; Zidan, R.; Mariels, N.; Hee, A.; Hagen, C. *Int. J. Hydrogen Energy* **1999**, *24*, 461. (b) Zidan, R. A.; Takara, S.; Hee, A. G.; Jensen, C. M. *J. Alloys Compd.* **1999**, *285*, 119. (c) Jensen, C. M.; Gross, K. J. *Appl. Phys. A* **2001**, *72*, 213.

(16) Gross, K. J.; Guthrie, S.; Takara, S.; Thomas, G. *J. Alloys Compd.* **2000**, *297*, 270.

(17) (a) Hout, J.; Boily, S.; Guther, V.; Schulz, R. *J. Alloys Compd.* **1999**, *283*, 304. (b) Zaluski, L.; Zaluska, A.; Strom-Olsen, J. O. *J. Alloys Compd.* **1999**, *290*, 71. (c) Balema, V. P.; Pecharsky, V. K.; Dennis, K. W. *J. Alloys Compd.* **2000**, *313*, 69.

(18) (a) Zakharkin, L. I.; Gavrilenko, V. V. *Dokl. Akad. Nauk SSSR* **1962**, *145*, 793. (b) Ashby, E. C.; Kobetz, P. *Inorg. Chem.* **1966**, *5*, 1615. (c) Bastide, J. P.; Bonnetot, B.; Létoffé, J. M.; Claudy, P. *Mater. Res. Bull.* **1981**, *16*, 91.

(19) Claudy, P.; Bonnetot, B.; Bastide, J. P.; Letoffe, J. M. *Mater. Res. Bull.* **1982**, *17*, 1499.

(20) Olofsson-Mårtensson, M.; Häussermann, U.; Tomkinson, J.; Noréus, D. *J. Am. Chem. Soc.* **2000,** *122*, 6960.

(21) Balema, V. P.; Dennis, K. W.; Pecharsky, V. K. *Chem. Commun.* **2000**, 1665.

(22) Klug, H. P.; Alexander, L. E. *X-ray Diffraction Procedures*; John Wiley: New York, 1974.

(23) Hellstern, E.; Fecht, H. J.; Fu, Z.; Johnson, W. L. *J. Appl. Phys.* **1989**, *65*, 305.

(24) (a) Haber, J. A.; Crane, J. L.; Buhro, W. E.; Frey, C. A.; Sastry, S. M. L.; Balbach, J. J.; Conradi, M. S. *Adv. Mater.* **1996**, *8*, 163. (b) Haber, J. A.; Gunda, N. V.; Balbach, J. J.; Conradi, M. S.; Buhro, W. E. *Chem. Mater.* **2000**, *12*, 973.

(25) (a) Garner, W. E.; Haycock, E. W. *Pro. Roc. Soc. Ser. A* **1952**, *211*, 335. (b) Mikheeva, V. I.; Selivokhina, M. S.; Kryukova, O. N. *Dokl. Akad. Nauk SSSR* **1956**, *109*, 439. (c) Block, J.; Gray, A. P. *Inorg. Chem.* **1965**, *4*, 304.

(26) (a) Dilts, J. A.; Ashby, E. C. *Inorg. Chem.* **1972**, *11*, 1230. (b) Bastide, J. P.; Bonnetot, B.; Letoffe, J. M.; Claudy, P. *Mater. Res. Bull.* **1985**, *20*, 997.

(27) (a) Raichlen, J. S.; Doremus, R. H. *J. Appl. Phys.* **1971**, *42*, 3166. (b) Tanaka, S.; Clewley, J. D.; Flanagan, T. B. *J. Phys. Chem.* **1977**, *81*, 1684.

(28) Sandrock, G.; Gross, K.; Thomas, G.; Jensen, C.; Meeker, D.; Takara, S. *J. Alloys Compd.*, in press.

(29) Dymova, T. N.; Aleksandrov, D. P.; Konoplev, V. N.; Silina, T. A.; Sizareva, A. S. *Russ. J. Coord. Chem.* **1994**, *20*, 263.

(30) Wang, G. W.; Komatsu, K.; Murata, Y.; Shiro, M. *Nature* **1997**, *387*, 583.

(31) Mikheeva, V. I.; Arkhipov, S. M. *Russ. J. Inorg. Chem.* **1967**, *12*, 1066.

(32) Aronson, S.; Salzano, F. J. *Inorg. Chem.* **1969**, *8*, 1541.

(33) Sanjinés, R.; Tang, H.; Berger, H.; Gozzo, F.; Margaritondo, G.; Lvéy, F. *J. Appl. Phys.* **1994**, *75*, 2945.

(34) (a) Henderson, M. A. *Langmuir* **1996**, *12*, 5093. (b) Wang, R.; Sakai, N.; Fujishima, A.; Watanabe, T.; Hashimoto, K. *J. Phys. Chem. B* **1999**, *103*, 2188.

(35) Schlapbach, L.; Riesterer, T. *Appl. Phys. A* **1983,** *32*, 169.

(36) Buschow, K. H. J. In *Handbook on the Physics and Chemistry of Rare Earths*; Gschneidner, K. A., Jr., Eyring, L., Eds.; Elsevier Science: Amsterdam, 1984; Vol. 6, p 1.

(37) (a) Sinke, G. C.; Walker, L. C.; Oetting, F. L.; Stull, D. R. *J. Chem. Phys.* **1967**, *47*, 2759. (b) Turley, J. W.; Rinn, H. W. *Inorg. Chem.* **1969**, *8*, 18.

(38) Bastide, J. P.; Bureau, J. C.; Letoffe, J. M.; Claudy, P. *Mater. Res. Bull.* **1987**, *22*, 185.

(39) Gunn, S. R.; Green, L. G. *J. Am. Chem. Soc.* **1958**, *80*, 4782.